Energy Materials and Devices

Research Article

Laboratory-based X-ray diffractometer with fast time resolution for *operando* battery studies

Zhenzhong Li, Chao Wang, Fanqiang Meng, Zhou Zhou, Lei Li, Chunzhen Yang ✉, and Dongbai Sun ✉

Graphical Abstract

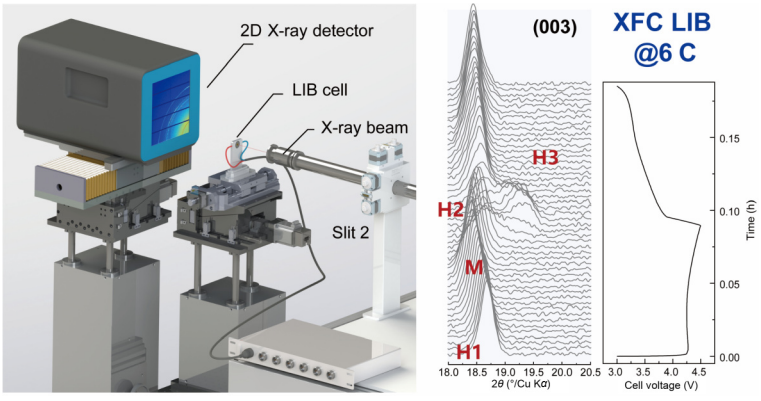

A laboratory X-ray source-based diffractometer with a high photon flux of 7.00×10^{8} photons/s and an energy resolution of 5.9×10^{-3} was fabricated. *Operando* X-ray diffraction measurements were performed to demonstrate the potential applications of the developed device in the study of fast charge–discharge lithium-ion batteries.

✉Address correspondence to Chunzhen Yang, yangchzh6@mail.sysu.edu.cn; Dongbai Sun, sundongbai@mail.sysu.edu.cn

Received: December 13, 2024
Revised: February 16, 2025
Accepted: February 26, 2025

Citation: Li Z., Wang C., Meng F., et al. Laboratory-based X-ray diffractometer with fast time resolution for *operando* battery studies. *Energy Mater. Devices*, 2025, 3(1), 9370057. https://doi.org/10.26599/EMD.2025.9370057

Energy Materials and Devices

Open Access

Research Article

https://doi.org/10.26599/EMD.2025.9370057

Laboratory-based X-ray diffractometer with fast time resolution for *operando* battery studies

Zhenzhong Li[1,2], Chao Wang[1], Fanqiang Meng[3], Zhou Zhou[4], Lei Li[2], Chunzhen Yang[1] ✉, and Dongbai Sun[5] ✉

[1] *School of Materials, Sun Yat-Sen University, Shenzhen 518107, China*
[2] *Institute of Advanced Science Facilities, Shenzhen 518107, China*
[3] *Sino-French Institute of Nuclear Engineering and Technology, Sun Yat-Sen University, Zhuhai 519082, China*
[4] *School of Physics, Sun Yat-Sen University, Guangzhou 510275, China*
[5] *School of Materials Science and Engineering, Sun Yat-Sen University, Guangzhou 510275, China*

Received: December 13, 2024 / **Revised:** February 16, 2025 / **Accepted:** February 26, 2025

ABSTRACT

Operando X-ray diffraction (XRD) is an important characterization tool for real-time monitoring of structural changes in materials under different reaction conditions. In this study, we developed a laboratory-based diffractometer that could capture a full XRD spectrum within 10 s. The instrument has several advanced features. First, it uses a Ga–In alloy metal-jet X-ray source, thereby achieving high X-ray flux with a brightness of up to 3.0 × 10^{10} photons/(s·mm^2·$mrad^2$). Second, it employs an ellipsoidal mirror with a multilayer coating to produce quasi-parallel monochromatic light characterized by a divergence of 0.6 mrad and an energy resolution of 5.9 × 10^{-3}. Third, it is equipped with a high-efficiency, high-signal-to-noise-ratio Pilatus 3R 1M detector for collecting diffraction signals. These features make the developed instrument applicable in studying rapid phase transitions in lithium-ion batteries, especially under extremely fast charge–discharge conditions. The data quality was comparable to that of synchrotron radiation XRD.

KEYWORDS

X-ray diffractometer, metal-jet X-ray source, extreme fast-charging battery, structure evolution, device assembly

1 Introduction

Since Max von Laue, a German physicist, obtained the first X-ray diffraction (XRD) pattern in 1912, XRD technology has undergone significant development, becoming increasingly sophisticated and convenient. Using technologies such as high-flux X-ray sources, high-speed low-noise X-ray detectors, and high-performance computing, modern X-ray diffractometers can achieve automated diffraction data collection and calibration. Current laboratory diffractometers can be classified into two main categories: powder XRD and single-crystal XRD[1–4]. The former uses reflection methods with a two-circle goniometer and point detector to collect diffraction signals, which are commonly used to analyze powder, bulk, and thin-film samples. The latter employs transmission methods using a multicircle goniometer and area detector to collect diffraction signals, which are used to determine single-crystal samples in chemical crystallography and structural biology. Combined with the increasingly refined standard diffraction databases, users can quickly obtain information about the phase composition and crystal structure of samples. With recent innovations in large-area and high-efficiency detector technologies, the two-dimensional (2D)-XRD technique, which is characterized by rapid time resolution, has attracted significant attention. 2D-XRD employs area detectors to directly capture 2D diffraction signals within a certain angular range of the Ewald sphere of a

✉Address correspondence to Chunzhen Yang, yangchzh6@mail.sysu.edu.cn; Dongbai Sun, sundongbai@mail.sysu.edu.cn

sample. The acquired 2D diffraction patterns can directly display the positions and intensities of the diffraction peaks corresponding to various crystal planes within the sample. After calibration and integration processing using standard samples, the 2D diffraction patterns provide crucial information about the crystal structure of the material, including the lattice parameters and crystal plane orientation. When combined with *operando* experimental setups, 2D-XRD enables various time-resolved *operando* experiments, serving as a powerful tool for dynamic observation of the evolution of sample microstructures.

The development of electrode materials for next-generation batteries with rapid charge–discharge capacity requires *operando* XRD devices with fast time resolution to study their lattice parameters, phase transitions, and rapid volume changes during fast charge–discharge processes[5]. However, conventional commercial XRD instruments are limited by low incident flux and narrow detector acceptance angle ranges, which makes it impossible to obtain fast time resolution for a wide range of diffraction spectra (diffraction signal ranges exceeding 30°) during *operando* signal acquisition. Compared with laboratory XRD, synchrotron radiation (SR) XRD is effective for rapid and precise crystal structure analysis, *in situ* dynamic monitoring, and microregion analysis because of its high-brightness, high-energy, high-resolution, and broad spectral range. It is particularly suitable for high signal-to-noise ratio (SNR) data collection and microstructural analysis, which are difficult with conventional XRD.

SR light sources are high-precision, high-performance scientific facilities with potential applications across various fields. However, their applications have been limited by time allocation and beam time scarcity, which do not meet the growing scientific demands. With the increasing demand for advanced X-ray characterization, the shortage in the SR beam time has become more pronounced. Moreover, the high construction and operational costs of SR light sources further limit their widespread use in industrial research and development (R&D). For small- and medium-sized enterprises, the cost of using such facilities is often high, making it difficult to integrate them into R&D processes. Some synchrotron facilities have built dedicated industrial application beamlines to systematically and continuously overcome core technological challenges in the industry. The urgent demand for laboratory-based high-throughput and fast time-resolved XRD has also prompted us to develop a 2D-XRD diffractometer using a Ga–In alloy metal-jet X-ray source with ultrahigh brightness.

2 Instrument design and assembly

The quality of 2D-XRD data is determined by the beam divergence and spot size at the sample position, as well as by the pixel size and SNR of the detector. A nearly parallel submillimeter beam and a detector with a small pixel size and high SNR can effectively enhance data quality. Under the same conditions, an increase in photon flux at the sample position enhances the temporal resolution of the instrument. The instrument design focuses on obtaining the highest possible photon flux while meeting the beam requirements for 2D-XRD analysis, thereby maximizing the improvement in the temporal resolution.

Figure 1 shows the conceptual design of the proposed laboratory-based X-ray diffractometer. This advanced X-ray diffractometer was supported and funded by the Institute of Advanced Science Facilities (IASF) in Shenzhen, thus, we named it IASF-XRD. One of the key features of the device is that it uses a high-brightness Ga–In alloy metal-jet X-ray source, a type of X-ray generator that uses a liquid-metal jet or droplet target made from Ga–In alloy. The Ga–In alloy serves as a target and is bombarded with high-energy electrons. When the electrons hit the liquid-metal target, they rapidly decelerate, and the kinetic energy is converted into X-ray photons via inverse Compton scattering or bremsstrahlung. The advantages of using a Ga–In alloy metal-jet X-ray source include high-brightness and tuneable spectral properties. The X-ray beam emitted by the source undergoes monochromatization and collimation through a reflecting mirror with a multilayer coating. Before it was incident on the sample, the X-

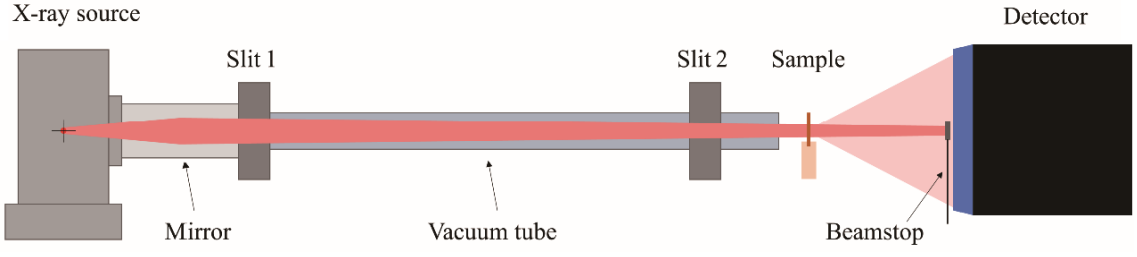

Figure 1 Conceptual design of the proposed IASF-XRD. The primary components of this XRD instrument are as follows: a high-performance X-ray source, a focusing mirror, slits, a vacuum channel, and a 2D X-ray detector. A beamstop is positioned between the sample and detector to shield the center of the detector from overexposure to X-rays.

ray beam was constrained by two sets of slits to achieve different divergences to meet various experimental requirements. A 2D detector is positioned at the beam focus plane behind the sample to collect the diffraction signals. Each component will be elaborately described below.

2.1 X-ray Source

The developed XRD instrument has a metal-jet X-ray source (eXcillum MetalJet D2+ 70 kV) with a Ga–In alloy (ExAlloy-G1 with a mass ratio Ga 95%:In 5%) liquid-metal jet as the anode. The Kα characteristic energy of Ga is 9240 eV, which is slightly higher than that of Cu. Unlike traditional solid-anode X-ray sources, liquid-metal anodes are not limited by the need to maintain the target material at temperatures far below its melting point. Thus, they can withstand power densities exceeding 1000 kW/mm^2 under a 10 μm-diameter electron beam. Combining this exceptionally high-power loading capacity with a small electron focal spot, MetalJet D2+ can emit X-rays with a brightness of 3×10^{10} photons/(s·mm^2·mrad^2) at a spot size of 20 μm × 80 μm (vertical × horizontal) under an excitation voltage of 70 kV[6]. The metal-jet X-ray source has a filament lifespan comparable to that of a rotating-target source (~2000 h). However, because of its more intricate design, replacing the filament necessitates the simultaneous replacement of some components, such as liquid-metal nozzles, filters, and windows, thereby incurring higher maintenance costs.

2.2 Optical design

To ensure high collimation of incident X-rays on the sample while maximizing the photon flux and taking full advantage of the small vertical beam size of the metal-jet X-ray source, the developed diffractometer incorporates a horizontally positioned ellipsoidal focusing mirror that focuses the beam onto the detector plane. Two sets of antiscatter slits are installed behind the focusing mirror to collimate the beam and remove stray light. Figure 2a shows the optical path geometry of the device. The ellipsoidal mirror has an effective length of 65 mm, width of 15 mm, and compression ratio of 1:10. The graded multilayer structure comprises 60 alternating layers with a central d-spacing of 3.955 nm. This is achieved using molybdenum (Mo) layers with a d-spacing of 1.810 nm and silicon (Si) layers with a d-spacing of 2.135 nm, resulting in a $d_{Mo}/(d_{Mo}+d_{Si})$ (Γ-ratio) of 0.46[7]. Using the OASYS software[8], the reflectance curve of the multilayer-coated mirror near 9240 eV is calculated for an incidence angle of 1.01°, as shown in Fig. 2b. The incident angle and finite size of the mirrors determine the acceptance angle. A larger acceptance angle results in a higher photon flux at the sample but reduces the resolution of the diffractometer, which is affected by beam divergence (detailed discussion in Section 3.4). The large incident angle (1.01°) of the multilayer mirror provides an unprecedented photon flux in the optical path. For comparison, in the same optical geometry, the acceptance angles of the Si and Pt coatings are 0.18° and 0.38°, respectively. Theoretically, after reflection from the multilayer-coated mirror, a monochromatic X-ray with a bandwidth as narrow as 261 eV at full width at half maximum (FWHM) can be obtained.

2.3 Detector

To efficiently collect diffraction signals from the sample and improve the time resolution of the experiment, the diffractometer utilizes a Pilatus 3R 1M pixel array detector from Dectris. The main technical parameters of Pilatus 3R 1M are listed in Table 1[9]. The detector is mounted on an *XYZ* displacement stage, allowing for specific position adjustments based on the test requirements.

2.4 Assembly of the diffractometer

As shown in Fig. 3, the assembled IASF-XRD comprises three major parts: the light source system (on the right), the sample stage system (in the center), and the detector system (on the left).

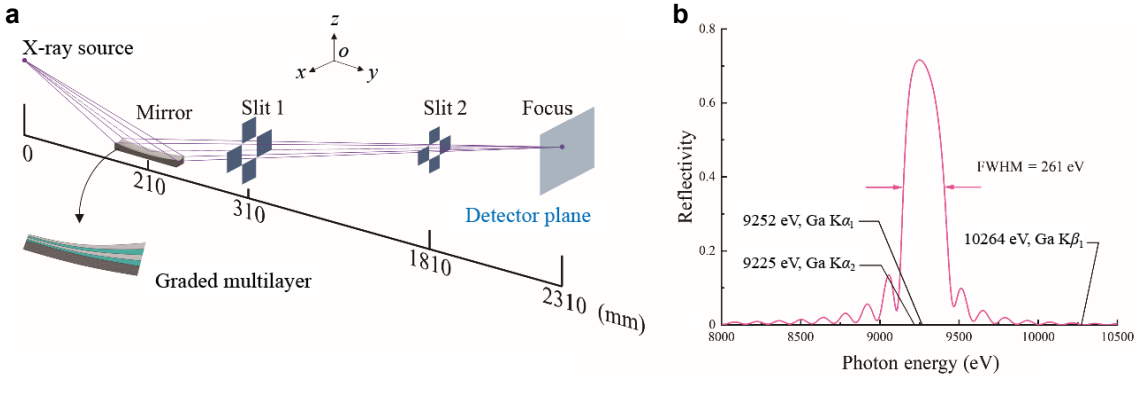

Figure 2 X-ray optical path design. (a) Schematic of the optical path geometry. (b) Reflectance curve of the multilayer coatings near 9240 eV at an incidence angle of 1.01°.

Table 1 Main technical parameters of Pilatus 3R 1M[9]

Technical specification	
Sensor material	Si
Pixel size ($W \times H$)	172 μm × 172 μm
Energy range	5–36 keV
Pixel array format ($W \times H$)	981 pixels × 1043 pixels
Image bit depth	32 bit
Maximum count rate	1×10^7 photons/s per pixel
Maximum frame rate	5 Hz

The MetalJet X-ray source is installed on the left optical platform. The X-ray beam output of the source is directed toward an ellipsoidal mirror (from Xenocs FOX3D Ga). Behind the mirror is a vacuum pipeline, along which two sets of antiscatter slits (from Xenocs) are arranged. At the output of the vacuum pipeline, multistage detachable quick-release vacuum pipes are installed to accommodate different sample environment setups, thereby minimizing the air path and improving SNR.

The sample stage system comprises three adjacent platforms with different functionalities: a hexapod sample stage, a conventional scanning sample stage (Stage 2), and a θ–2θ sample stage, where θ specifically represents the X-ray incident angle (from HUBER 416A). These three platforms can be switched for use. Thus, we describe only the conventional Stage 2. The Stage 2 platform has an X-axis travel of 120 mm with a repeatable positioning accuracy of ±10 μm and a Z-axis travel of 50 mm with a repeatable positioning accuracy of ±5 μm. It can perform experiments, such as scanning at different positions of a single bulk sample and automatic testing of multiple samples, thus, it meets the requirements for transmission XRD analyses.

The detector system comprises a Pilatus 3R 1M detector and an XYZ displacement stage for position adjustment. Both the X and Z displacement stages have a travel range of 200 mm with a repeatable positioning accuracy of ±50 μm and can direct the incident beam to any position on the detector. The Y direction is equipped with a manual sliding stage, allowing the distance between the detector and sample to be adjusted according to the experimental requirements (with a minimum of 120 mm).

3 Results and discussion

We tested various performance parameters of the assembled diffractometer using different methods, as discussed below.

3.1 Energy resolution

The energy resolution of an XRD instrument is a critical parameter that determines the ability to distinguish between closely spaced X-ray wavelengths and energies. It is expressed as the FWHM of the diffracted peak or as the ratio of the width of the peak ΔE to the central energy E of the X-ray source[10]. Higher energy resolution allows for more accurate identification of the crystal structures and phases of a material, as well as the ability to detect subtle changes in the material structure. This is particularly impor-

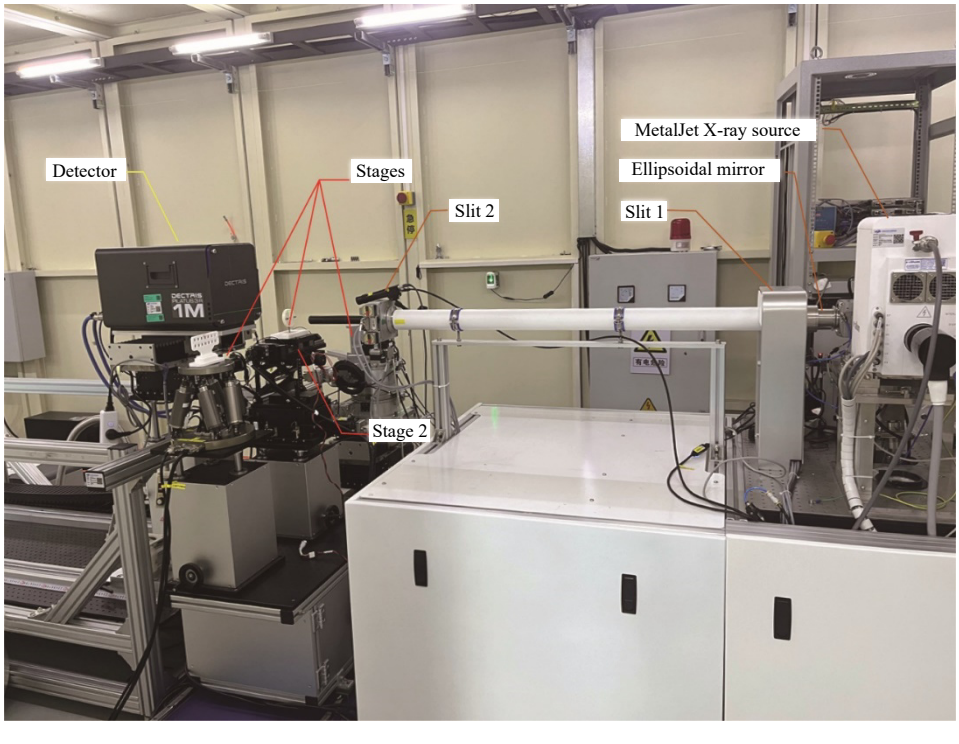

Figure 3 Layout of the IASF-XRD instrument.

tant in research and quality control, where precise analyses are required.

To determine the energy resolution of IASF-XRD, a single-crystal Si(111) was placed on the high-precision rotary stage. By continuously rotating the single-crystal Si and measuring the diffraction intensity of the Si(111) plane at varying incident angles, the rocking curve of the single-crystal Si was captured by the photodiode detector. This curve represents the variation in the diffracted X-ray intensity with the angle of incidence. Figure 4a shows the experimental setup for this procedure.

As shown in Fig. 4b, the rocking curve was fitted with a double Gaussian peak model, and peaks were observed at 9250 and 9228 eV. These peak positions agree well with the characteristic energies of the Ga $K\alpha_1$ line (9252 eV) and $K\alpha_2$ line (9225 eV). FWHM of the rocking curve was 55 eV and the energy resolution of the X-ray source, calculated as $\Delta E/E$, was approximately 5.9×10^{-3}.

3.2 X-ray beam divergence

The angular dispersion of the X-ray beam originating from the source is a key parameter known as beam divergence. An ideal XRD setup uses a highly collimated beam with minimal divergence, thereby enhancing the precision of the diffraction measurements. Precise control over this divergence is essential for achieving high-resolution diffraction and clear diffraction patterns, whereas inadequate control may cause complications, such as peak overlap, weakened peak intensities, and peak broadening, which can obscure data analysis and interpretation.

Several common methods for testing the X-ray beam divergence have been reported[11,12]. Here, we employed the commonly used pinhole camera method. The slit aperture was adjusted to ensure that its edges serve solely to eliminate stray X-rays without impacting the primary X-ray beam. An EIGER 500K detector was positioned beyond the focal plane of the beam to capture images of the beam spot at various points along the beam trajectory. By analyzing the changes in the size of the beam spot with the test point positions, we estimated the X-ray beam divergence. Figure 4c shows this experimental setup.

The test results are shown in Fig. 4d. By linear fitting, the vertical divergence of the beam was determined as 0.6 mrad, and the horizontal divergence was 0.9 mrad. In actual testing, unless a very high-flux is required, experiments are typically conducted with the beam constrained by the slit to have both vertical and horizontal divergences of approximately 0.3 mrad.

In 2D-XRD performed in the transmission mode, a large beam size can significantly reduce the signal quality. To ensure high data quality, a 2D collimated submillimeter beam is required. The advantage of using the Ga–In alloy metal-jet X-ray source includes its ability to withstand extremely high-power-density electron beams due to its liquid state. This enables higher beam brightness with a small beam size, thereby meeting the time-resolution requirements of 2D-XRD.

3.3 Photon flux

Photon flux is another crucial parameter for XRD

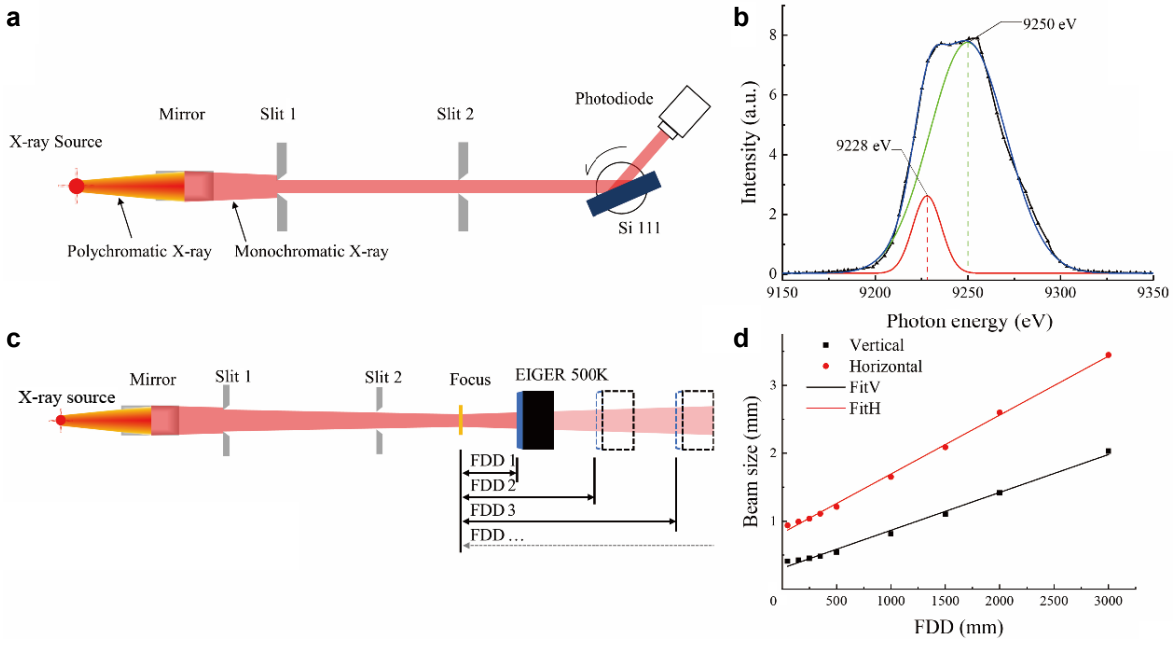

Figure 4 Evaluation of the performance parameters. (a) Schematic of the energy resolution test setup. (b) Rocking curve of Si(111). The curve is fitted with Ga Kα1 (green) and Kα2 (red) lines. (c) Schematic of divergence test setup. (d) Tested beam size and focus to detector distance (FDD).

analysis. It denotes the quantity of photons, which are particles of X-ray light, that pass through a given area per unit time[13]. It measures the intensity of an X-ray beam and is crucial for determining the quality and speed of XRD experiments. High photon fluxes can result in better SNR and faster data collection.

The photon flux can be verified using two methods. In the first method, the slit is adjusted to replicate the conditions of the above-mentioned beam divergence test. The first method employs a 400 μm aluminum (Al) foil to attenuate the primary X-ray beam flux, reducing it to 1/30 of its original intensity. Subsequently, the attenuated beam is directly exposed to an EIGER 500K detector, which can count single photons. By multiplying the total counts of the detector per unit time with an attenuation factor, the total photon flux of the original X-ray beam can be obtained. The second method utilizes a calibrated photodiode, specifically the Hamamatsu S13993 model, to directly measure the direct beam photon flux[14]. The excitation current from the photodiode is then converted to the photon flux value.

Upon completion of the tests, the results are cross-verified for accuracy. For the proposed diffractometer, the photon fluxes calculated using the area detector and photodiode methods were 7.14×10^8 and 7.51×10^8 photons/s, respectively. The values are close, indicating the reliability of both methods in evaluating the photon flux of the X-ray beam.

3.4 Data quality

Commercial diffractometers employ the reflection method to collect diffraction signals and use high-flux line beams and high-precision goniometers to achieve high SNR and resolution, respectively, thereby meeting the requirements of most powder diffraction analyses. In contrast, IASF-XRD collects diffraction signals using the transmission method. The application of a high-brightness metal-jet X-ray source not only meets the requirements for beam size and divergence essential for the transmission method but also in conjunction with area detectors, enables time-resolved measurements with second-level precision, which cannot be achieved by commercial diffractometers.

To further assess the data quality, we compared the data obtained from the IASF-XRD and SR-XRD beamlines. This comparison evaluates the performance and reliability of the IASF-XRD system by benchmarking it against the high-intensity and high-resolution capabilities of synchrotron-based XRD measurements.

The XRD standard sample, SRM 660c LaB_6, from China National Institute of Standards and Technology was tested using IASF-XRD and the BL16B1 beamline of the Shanghai SR Facility (SSRF) at the same energy (9240 eV). Figure 5a shows the obtained one-dimensional diffraction patterns after integration, with the IASF-XRD and SSRF results marked as "IASF" and "SSRF", respectively.

The FWHMs of the diffraction peaks at the five overlapping points were fitted to a Gaussian curve and compared with the results shown in Fig. 5b. In the low-angle region, the IASF-XRD and SSRF results are very close (ΔWidth = 0.06°). As the angle increased, the peaks in the IASF-XRD results significantly broadened. Compared with the SSRF, the peak at 46° in the IASF-XRD results is ~80% broader. In addition, peak splitting was observed in the IASF-XRD results, as shown in Fig. 5c. The slight differences in the low-angle region are primarily due to the differences in the monochromaticity of the incident beams. The energy resolution of the incident beam for IASF-XRD was 5.9×10^{-3}, whereas that for SSRF was 4×10^{-4} [15]. As the diffraction angle increased, the projection of the diffraction peaks on the detector plane broadened, as shown in Fig. 5d, allowing the detector to more clearly capture the shape of the diffraction peaks. The shape of the split peak shown in Fig. 5c aligns with the shape of the rocking curve in Fig. 5b. The peak broadening in the high-angle region can be attributed to the combined effects of beam divergence and the monochromaticity of the incident beam. Although the IASF-XRD data show a certain degree of peak broadening, the accuracy of the peak positions remaines unchanged. This allows for *in situ* experiments that focus on changes in peak positions.

3.5 Time resolution capacity

Lithium-ion batteries (LIBs) are essential components of electric vehicles (EVs), playing a crucial role in enhancing EV performance and market expansion[16,17]. Currently, the primary challenge facing EV development is the battery capacity and fast-charging ability. The charging time for EVs significantly exceeds refueling time for internal combustion engine vehicles. To address this, USA Department of Energy has introduced the concept of "extremely fast-charging" (XFC) for LIBs, which is defined as the ability to recharge up to 80% of the battery capacity within 15 min[18–20]. This phenomenon has attracted significant attention[21,22]. However, the development of fast-charging LIBs is hindered by the low rate of Li^+ transport and the associated phase transitions at the cathode. Ni–Co–Mn (NCM) cathode materials undergo significant lattice variations during charge–discharge cycles. Such structural changes are accompanied by shifts in the lattice parameters and the generation of internal lattice stress, which result in the structural degradation of the cathodes and reduce the battery performance[23–26].

An XFC LIB completely charges within 15 min.

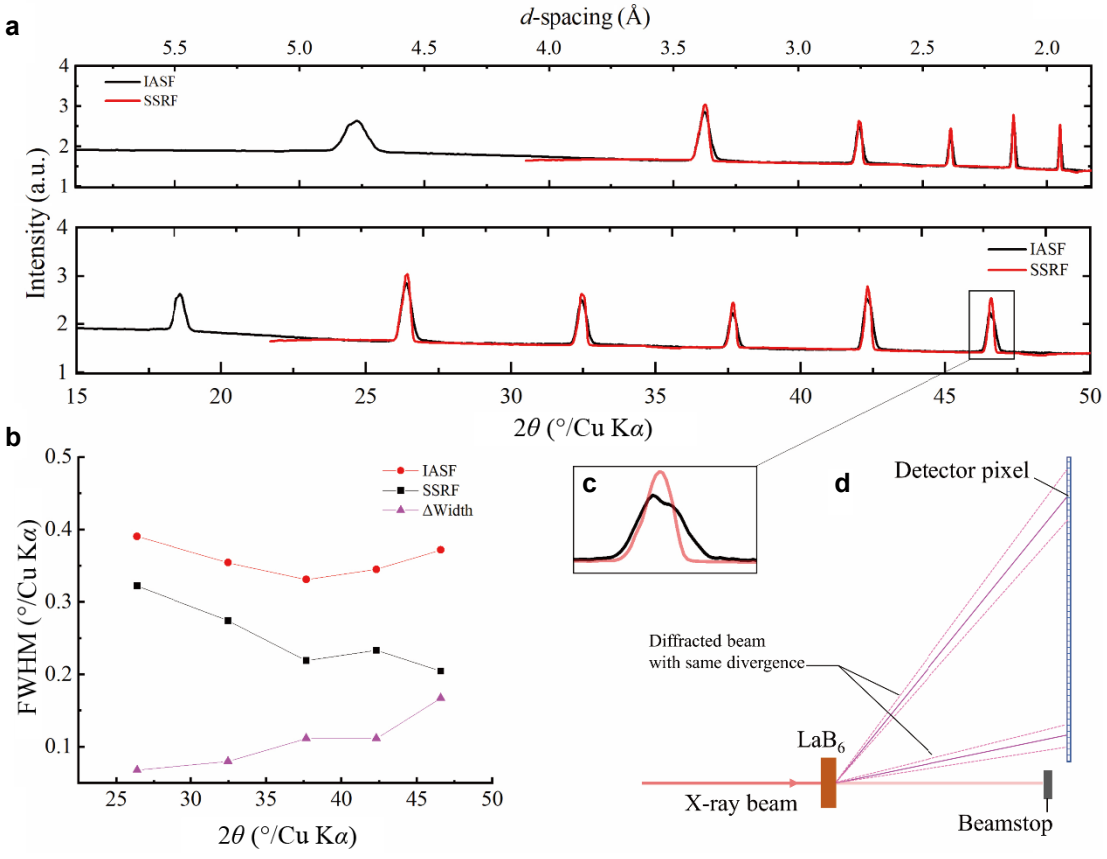

Figure 5 Evaluation of the XRD spectral quality. (a) Comparison between LaB_6 diffraction patterns obtained from IASF-XRD and SSRF XRD beamline. (b) Comparison of the FWHM values of different diffraction peaks. (c) Magnified peaks in the high-angle region. (d) Mechanism of the diffracted beam collected on the IASF-XRD instrument at high angles.

However, most commercial laboratory-scale X-ray diffractometers cannot capture such rapid processes. Thus, SR light sources are usually employed. However, the available testing time at SR light sources is very limited, which is not conducive to academic research. Therefore, there is a need to develop XRD instruments with high X-ray fluxes and rapid time resolution.

In this study, the layered cathode material, $LiNi_{0.92}Co_{0.05}Mn_{0.03}O_2$ (NCM92), which is widely used in commercial LIBs, was used as a test sample to verify the time-resolved testing ability of IASF-XRD. NCM92 powder was encapsulated in 50 μm-thick flat sheets using a 25 μm-thick Kapton. The same samples were tested using the IASF-XRD and Bruker D8 Advance diffractometer in both transmission and reflection modes under different exposure times to compare data quality. IASF-XRD was operated in the transmission mode, where single exposures directly captured diffraction signals in the 10°–50° range. For the Bruker D8 Advance diffractometer, experiments were conducted in the θ–θ scanning mode with a step size of 0.02°, covering a scanning range of 10°–50°. The commercial Bruker D8 Advance diffractometer was equipped with an SDD160-2 X-ray detector.

Figure 6 shows the effect of test duration on the XRD data quality, which is crucial for accessing the time resolution and reliability of XRD data when applied to *operando* XRD analysis of LIBs. As shown in Fig. 6b, under the same conditions, the XRD patterns obtained from IASF-XRD under a 10 s exposure are comparable with those obtained from Bruker D8 under a 10 min exposure. This result highlights the efficiency of IASF-XRD in acquiring comparable data quality in a significantly shorter time frame.

Here, we summarize the results of the IASF-XRD performance tests to obtain the main performance parameters. IASF-XRD outperformed other custom-built 2D-XRD diffractometers that used multilayer mirrors[27,28] in terms of X-ray photon flux (Table 2). As shown in Fig. 6, IASF-XRD achieved a time resolution of only 10 s, outperforming the widely used Bruker D8 diffractometer.

3.6 *Operando* XRD results

With the extensive development of power batteries for fast-charging purposes, the ability of a battery to complete charging within a few minutes has become crucial. Extremely fast charge and discharge (with charge/discharge rate > 4 C) pose significant challenges to the structural stability of battery cathode materials[18–20]. Under XFC conditions, LIB cathode

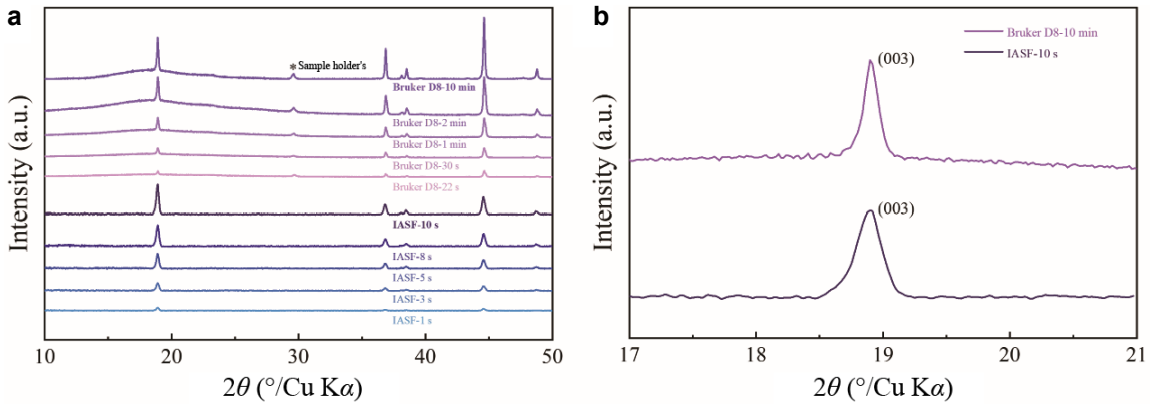

Figure 6 Time resolution of the XRD spectra. (a) Comparison of the diffraction patterns of $LiNi_{0.6}Co_{0.2}Mn_{0.2}O_2$ captured at different test durations. (b) Comparison of the (003) diffraction peaks captured using a Bruker D8 Advance for 10 min and IASF-XRD for 10 s.

Table 2 Parameter comparison

Parameters	Energy (keV)	Energy bandwidth (eV)	Photon flux (photons/s)
IASF-XRD	9.25	55 (Ga $K\alpha_1 + K\alpha_2$)	7×10^8
KIT-XRD[27]	17.45	150 (Mo $K\alpha_1 + K\alpha_2$)	1×10^8
TAU-XRD[28]	8.05	40 (Cu $K\alpha_1 + K\alpha_2$)	5×10^7
SSRF (BL16B1)	4–20	2 eV@10 keV (Si (111))	3×10^{11}@10 keV

materials undergo rapid Li^+ extraction and insertion processes, which can result in structural degradation and performance decline. The crystal structure, lattice parameters, and phase transitions of cathode materials are key factors that affect the performance of LIBs under XFC conditions. Investigating the rapid phase transition processes in batteries under XFC conditions requires a fast XRD signal acquisition capability that enables XRD measurements on a second scale, which is not achievable with most laboratory-based XRD instruments. To demonstrate the powerful time-resolution capacity of IASF-XRD, we conducted *operando* XRD tests for XFC batteries.

Operando XRD was performed using a CR2032 coin cell with a central aperture with a diameter of 3 mm[29]. The aperture was sealed with a 25 μm-thick Kapton film, allowing for the transmission of X-rays while maintaining the integrity of the cell. Figures 7a and 7b show the *operando* XRD test platform and the internal structure of the assembled Li^+ cell. The LIB cell was assembled in an argon-filled glovebox.

Before the *operando* XRD tests, the assembled Li^+ cell was precisely aligned with the optical path using a motorized translation stage. Upon confirmation of unobstructed preexposure diffraction images and stable diffraction signal intensity, automatic exposure and charge–discharge processes were initiated simultaneously. To facilitate time-resolved analysis, the diffraction patterns and electrochemical data were recorded using synchronized time stamps, enabling the precise temporal correlation between the structural evolution and electrochemical performance.

Figure 7c shows the *operando* XRD patterns of the NCM92 cathode material in a cut-off voltage range of 3.0 to 4.5 V. To demonstrate the superior time resolution of IASF-XRD, we performed *operando* XRD measurements under an XFC condition at a high charging rate of 6 C. This implies that LIB is charged from 3.0 to 4.5 V within 10 min. Each XRD pattern was captured with an exposure period of 10 s by the 2D detector. Furthermore, the full XRD spectrum was captured in a 2θ range of 10°–55°. The evolution of several characteristic diffraction peaks, indexed to the (003), (101), (104), and (015) crystal facets, can be observed.

The pristine NCM92 oxide exhibited a typical hexagonal α-$NaFeO_2$ structure with the R-3m space group. This hexagonal structure is denoted as H1. The NCM92 cathode material demonstrated superior structural reversibility during the initial three charge–discharge cycles. The evolution of the (003) diffraction peak during the second charge–discharge cycle, as highlighted by the dashed yellow box in Fig. 7c, was plotted. The (003) diffraction peak can be used to estimate the *d*-spacing of the layered M–O slabs. Upon charging, the *d*-spacing is initially expanded because of the removal of Li^+ from the layered structure. During this stage, the layered structure evolves from the hexagonal phase H1 to a monoclinic phase M and another hexagonal phase H2. Further extraction of Li^+ causes the shrinkage of the *d*-spacing and contraction of the unit-cell volume, resulting in the formation of the H3 phase. The H3 phase forms when the lithium content within the cathode material is reduced to a certain threshold

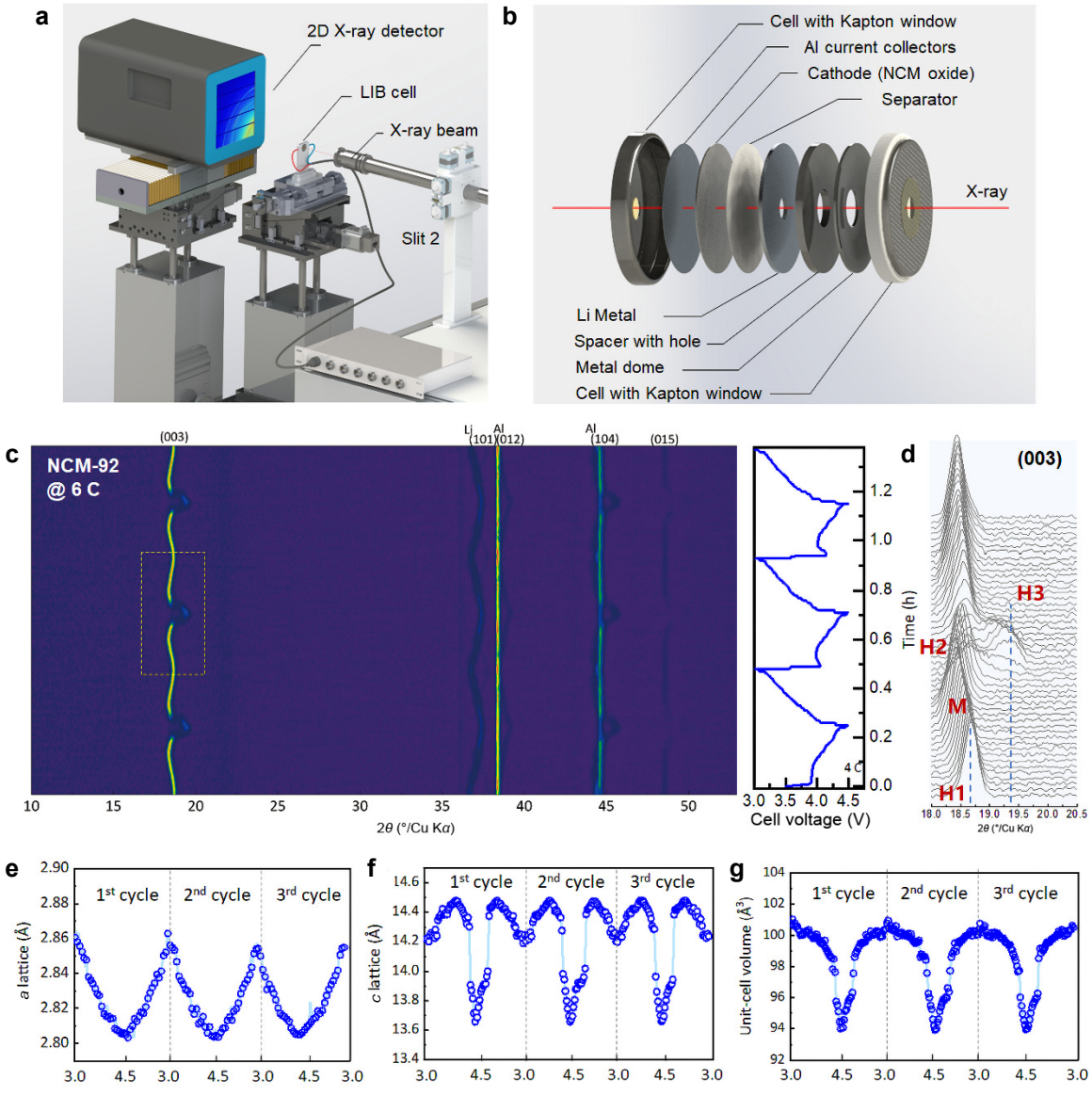

Figure 7 *Operando* XRD measurements for LIBs. (a) Schematic of the test platform for *the operando* XRD measurements. (b) Assembly of the *operando* Li^+ cell. (c) XRD patterns of the NCM92 cathode material during charge and discharge at a current rate of 6 C for three cycles. (d) Evolution of the (003) diffraction peaks (dashed yellow box) during the second charge–discharge cycle. Evolution of the *a* lattice parameter (e), *c* lattice parameter (f), and unit-cell volume (g) based on the batch fitting of the XRD profiles.

during charging, as reported for other high-Ni-content NCM cathodes[30,31].

The lattice parameters of the NCM layered structure were derived from the *operando* XRD profiles[32]. Figures 7e–7g show the evolutions of the *c*-axis, *a*-axis, and unit-cell volume. Throughout the high-rate charge–discharge process, the cell volume and *a*-axis lattice of NCM92 decreased as Li^+ delithiated from the layered structure. The *c*-axis significantly decreased by approximately 0.9 Å during the H2-to-H3 phase transformation. The significant changes in the lattice structure resulted in the buildup of internal structural stress, which was detrimental to the long-term stability of the crystal structure. This can result in the cracking and pulverization of NCM particle polymorphs during cycling.

Overall, these results underscore the ability of 2D-XRD with high temporal resolution to precisely capture the rapid phase transitions that occur in electrode materials even under extremely fast charge/discharge rates. Notably, *operando* XRD tests cannot be performed using commercial laboratory-based XRD instruments that employ Cu targets as X-ray sources. Therefore, IASF-XRD is a valuable and precise tool for monitoring the structural dynamics of batteries under XFC operational conditions.

4 Conclusion

We developed an advanced laboratory-based XRD instrument, IASF-XRD, that incorporated a Ga–In

alloy metal-jet X-ray source and a Pilatus 3R 1M area detector. By optimizing the optical paths, IASF-XRD delivers a high-quality X-ray beam with a maximum photon flux of 7×10^8 photons/s, minimum divergence of 0.1 mrad, and optimal energy resolution of 5.9×10^{-3}. To validate the data quality, we compared the XRD spectra obtained using IASF-XRD with the SR-XRD obtained at SSRF. Although the standard sample test results indicated peak broadening in the spectra obtained using IASF-XRD, the peak positions were consistent with those of the SR-XRD data. In addition, the data quality obtained in 10 s using IASF-XRD was comparable to that obtained in 10 min using the commercial laboratory-scale diffractometer.

Due to high photon flux and fast data acquisition capacity, IASF-XRD is suitable for investigating rapid phase transition mechanisms, e.g., the structure evolutions of electrode materials under high-rate charge/discharge conditions in power batteries. *Operando* XRD experiments were conducted on a widely used NCM cathode material for LIBs at a high charging rate of 6 C. The results show that the developed diffractometer can provide detailed insights into the dynamic structural changes in battery materials during rapid charge–discharge processes.

The single-reflection multilayer collimating mirror employed in IASF-XRD achieves a high-flux X-ray beam suitable for *in situ* experiments. However, it reduces the beam's monochromaticity and parallelism. Therefore, IASF-XRD is well-suited for observing phase changes in materials with known phases but less suitable for discovering new phases or precise lattice parameter calculations.

Acknowledgements

ChunzhenYang thanks BL14B1 and 16B1 beamline of SSRF for providing synchrotron beam time. Authors also thank Dr. Mu Li and Dr. Xiang Shi for their help in experiment and data analysis.

Author contribution statement

Writing—original draft: Zhenzhong Li and Chao Wang. Assembly: Zhenzhong Li, Fanqiang Meng, Zhou Zhou, Lei Li, and Chunzhen Yang. Writing—review and editing: Zhenzhong Li and Chunzhen Yang. Funding acquisition: Dongbai Sun and Zhou Zhou. All the authors have read and approved the final manuscript.

Data availability

The data that support the findings of this study is available from the corresponding author upon reasonable request.

Declaration of competing interest

All the contributing authors report no conflicts of interest in this work.

Funding

This work is financially supported by "2020 Special Fund for Key Technology and Equipment Development of Major Science and Technology Infrastructure" from the Development and Reform Commission of Shenzhen. Zhou Zhou would like to acknowledge financial support from National Natural Science Foundation of China (Grant No. 52103365) and Guangdong Innovative and Entrepreneurial Research Team Program (Grant No. 2021ZT09L227).

Use of AI statement

None.

References

[1] Guideline, I., Forensic, N. A. R., Intern, S. (2017). In Itwg Guideline on Powder X-Ray Diffraction (XRD)—General Overview. Roubaix: Nuclear Forensics International Technical Working Group.

[2] Echevarria-Bonet, C. (2014). Size induced electronic and magnetic changes in nanometric Rare Earth alloys. Ph.D. Dissertation. University of Oviedo, Oviedo, Spain.

[3] Altomare, A., Cuocci, C., Gatta, G. D., Moliterni, A., Rizzi, R. (2017). Methods of crystallography: Powder X-ray diffraction. *EMU Notes Mineral.* 29, 79–138.

[4] Hofbauer, S., Brito, J. A., Mulchande, J., Nogly, P., Pessanha, M., Moreira, R., Archer, M. (2015). Stabilization of porcine pancreatic elastase crystals by glutaraldehyde cross-linking. *Acta Crystallogr. Sect. F: Struct. Biol. Commun.* 71, 1346–1351.

[5] Li, H. Y., Guo, S. H., Zhou, H. S. (2021). *In-situ*/*operando* characterization techniques in lithium-ion batteries and beyond. *J. Energy Chem.* 59, 191–211.

[6] Hallstedt, J., Espes, E., Lundstrom, U., Hansson, B. (2018). In Liquid-Metal-Jet X-Ray Technology for Nanoelectronics Characterization and Metrology. In Proceedings of 2018 29th Annual SEMI Advanced Semiconductor Manufacturing Conference (ASMC), Saratoga Springs, NY, USA, p 151–154.

[7] Troussel, P., Dennetiere, D., Maroni, R., Høghøj, P., Hedacq, S., Cibik, L., Krumrey, M. (2014). Multilayer optics for monochromatic high-resolution X-ray imaging diagnostic in a broad photon energy range from 2 keV to 22 keV. *Nucl. Instrum. Methods Phys. Res. Sect. A: Accel., Spectrom, Detect., Assoc. Equip.* 767, 1–4.

[8] Rio, M. S. D., Rebuffi, L. (2019). OASYS: A software for beamline simulations and synchrotron virtual experiments. In Proceedings of the 13th International Conference on Synchrotron Radiation Instrumentation—Sri2018. Taipei, China, p 060081.

[9] DECTRIS. PILATUS3 R 1M Documentation. https://www.dectris.com/en/support/manuals-docs/pilatus3-r-for-laboratory/pilatus3-r-1m/ (accessed May 15, 2024).

[10] Midgley, S. (2006). Energy resolution for accurate measurements of the X-ray linear attenuation coefficient. *Radiat. Phys. Chem.* 75, 936–944.

[11] Nakae, M., Matsuyama, T., Ishi, H., Tsuji, K. (2023). Mathematical considerations for evaluating X-ray beam size in micro-XRF analysis. *X-Ray Spectrome.* 52, 290–302.

[12] Gherase, M. R., Vargas, A. F. (2017). Effective X-ray beam size measurements of an X-ray tube and polycapillary X-ray lens system using a scanning X-ray fluorescence method. *Nucl. Instrum. Methods Phys. Res. Sect. B: Beam Interact. Mater. At.* 395, 5–12.

[13] Owen, R. L., Holton, J. M., Schulze-Briese, C., Garman, E. F. (2009). Determination of X-ray flux using silicon pin diodes. *J. Synchrotron Radiat.* 16, 143–151.

[14] HAMAMATSU. Large-area Si PIN photodiode for direct radiation detection. https://www.hamamatsu.com/jp/en/product/optical-sensors/photodiodes/si-photodiodes/S13993.html (accessed May 15, 2024).

[15] Zeng, J., Bian, F., Wang, J., Li, X., Wang, Y., Tian, F., Zhou, P. (2017). Performance on absolute scattering intensity calibration and protein molecular weight determination at BL16B1, a dedicated SAXS beamline at SSRF. *J. Synchrotron Radiat.* 24, 509–520.

[16] Armand, M., Tarascon, J. M. (2008). Building better batteries. *Nature* 451, 652–657.

[17] Andre, D., Kim, S. J., Lamp, P., Lux, S. F., Maglia, F., Paschos, O., Stiaszny, B. (2015). Future generations of cathode materials: An automotive industry perspective. *J. Mater. Chem. A* 3, 6709–6732.

[18] Zhu, G. J., Luo, D. D., Chen, X. Y., Yang, J. P., Zhang, H. J. (2023). Emerging multiscale porous anodes toward fast charging lithium-ion batteries. *ACS Nano* 17, 20850–20874.

[19] Jin, H. C., Huang, Y. S., Wang, C. N., Ji, H. X. (2022). Phosphorus-based anodes for fast charging lithium-ion batteries: Challenges and opportunities. *Small Sci.* 2, 2200015.

[20] Chen, K. H., Goel, V., Namkoong, M. J., Wied, M., Müller, S., Wood, V., Sakamoto, J., Thornton, K., Dasgupta, N. P. (2021). Enabling 6 C fast charging of Li-ion batteries with graphite/hard carbon hybrid anodes. *Adv. Energy Mater.* 11, 2003336.

[21] Li, S. Q., Wang, K., Zhang, G. F., Li, S. N., Xu, Y. N., Zhang, X. D., Zhang, X., Zheng, S. H., Sun, X. Z., Ma, Y. W. (2022). Fast charging anode materials for lithium‐ion batteries: Current status and perspectives. *Adv. Funct. Mater.* 32, 2200796.

[22] Zhang, Z., Zhao, D. C., Xu, Y. Y., Liu, S. P., Xu, X. Y., Zhou, J., Gao, F., Tang, H., Wang, Z. L., Wu, Y. T., et al. (2022). A review on electrode materials of fast‐charging lithium‐ion batteries. *Chem. Rec.* 22, e202200127.

[23] Wu, F., Liu, N., Chen, L., Li, N., Dong, J. Y., Lu, Y., Tan, G. Q., Xu, M. Z., Cao, D. Y., Liu, Y. F., et al. (2021). The nature of irreversible phase transformation propagation in nickel-rich layered cathode for lithium-ion batteries. *J. Energy Chem.* 62, 351–358.

[24] Cui, S. H., Wei, Y., Liu, T. C., Deng, W. J., Hu, Z. X., Su, Y. T., Li, H., Li, M. F., Guo, H., Duan, Y. D., et al. (2016). Optimized temperature effect of Li-ion diffusion with layer distance in $Li(Ni_xMn_yCo_z)O_2$ cathode materials for high performance Li-ion battery. *Adv. Energy Mater.* 6, 1501309.

[25] Zou, L. F., Liu, Z. Y., Zhao, W. G., Jia, H. P., Zheng, J. M., Yang, Y., Wang, G. F., Zhang, J. G., Wang, C. M. (2018). Solid–liquid interfacial reaction trigged propagation of phase transition from surface into bulk lattice of Ni-rich layered cathode. *Chem. Mater.* 30, 7016–7026.

[26] Liao, J. Y., Manthiram, A. (2015). Surface-modified concentration-gradient Ni-rich layered oxide cathodes for high-energy lithium-ion batteries. *J. Power Sources* 282, 429–436.

[27] Geßwein, H., Stüble, P., Weber, D., Binder, J. R., Mönig, R. (2022). A multipurpose laboratory diffractometer for *operando* powder X-ray diffraction investigations of energy materials. *J. Appl. Crystallogr.* 55, 503–514.

[28] Gorfman, S., Spirito, D., Cohen, N., Siffalovic, P., Nadazdy, P., Li, Y. (2021). Multipurpose diffractometer for *in situ* X-ray crystallography of functional materials. *J. Appl. Crystallogr.* 54, 914–923.

[29] Wu, Z. B., Pang, W. K., Chen, L. B., Johannessen, B., Guo, Z. P. (2021). *In situ* synchrotron X‐ray absorption spectroscopy studies of anode materials for rechargeable batteries. *Batter. Supercaps* 4, 1547–1566.

[30] Yoon, C. S., Ryu, H. H., Park, G. T., Kim, J. H., Kim, K. H., Sun, Y. K. (2018). Extracting maximum capacity from Ni-rich $Li[Ni_{0.95}Co_{0.025}Mn_{0.025}]O_2$ cathodes for high-energy-density lithium-ion batteries. *J. Mater. Chem. A* 6, 4126–4132.

[31] Zhu, H., Tang, Y., Wiaderek, K. M., Borkiewicz, O. J., Ren, Y., Zhang, J., Ren, J. C., Fan, L. L., Li, C. C., Li, D. F., et al. (2021). Spontaneous strain buffer enables superior cycling stability in single-crystal nickel-rich NCM cathode. *Nano Lett.* 21, 9997–10005.

[32] Ryu, H. H., Park, K. J., Yoon, D. R., Aishova, A., Yoon, C. S., Sun, Y. K. (2019). $Li[Ni_{0.9}Co_{0.09}W_{0.01}]O_2$: A new type of layered oxide cathode with high cycling stability. *Adv. Energy Mater.* 9, 1902698.